

CVT-Based 3D Image Segmentation for Quality Tetrahedral Meshing

Kangkang Hu¹, Yongjie Jessica Zhang^{1(✉)}, and Guoliang Xu²

¹ Department of Mechanical Engineering, Carnegie Mellon University,
Pittsburgh, USA

{kangkanh,jessicaz}@andrew.cmu.edu

² LSEC, Institute of Computational Mathematics,
Academy of Mathematics and Systems Science,
Chinese Academy of Sciences, Beijing, China
xuguo@lsec.cc.ac.cn

Abstract. Given an input 3D image, in this paper we first segment it into several clusters by extending the 2D harmonic edge-weighted centroidal Voronoi tessellation (HEWCVT) method to the 3D image domain. The Dual Contouring method is then applied to construct tetrahedral meshes by analyzing both material change edges and interior edges. An anisotropic Giaquinta-Hildebrandt operator (GHO) based geometric flow method is developed to smooth the surface with both volume and surface features preserved. Optimization based smoothing and topological optimizations are also applied to improve the quality of tetrahedral meshes. We have verified our algorithms by applying them to several datasets.

Keywords: Centroidal voronoi tessellation · Image segmentation · Tetrahedral mesh · Quality improvement · Giaquinta-Hildebrandt operator

1 Introduction

Many methods have been developed for 2D/3D image segmentation in the literature [3, 13]. Thresholding [1, 18] is a very common approach which partitions the image based on the intensity values and a given threshold. Binarization was used in [19] to segment the raw image for accurate 3D reconstruction of the air exchange regions of the lung. *K*-means clustering [15] groups pixels in an image into non-overlapping clusters through the minimization of the total inter-cluster variance. Watershed [17] segments images into homogeneous regions by using concepts from edge detection and mathematical morphology. In recent years, centroidal Voronoi tessellation (CVT) has been extensively studied for image segmentation [5, 6], where the key idea is to partition the image by updating generators with respect to a specific energy function. The edge-weighted CVT (EWCVT) model [20] was proposed by incorporating spatial information into the energy function in order to eliminate the noises and unnecessary details.

The harmonic EWCVT (HEWCVT) model [9] extends EWCVT by introducing a harmonic form of clustering energy to generate more stable and accurate results. Starting from segmented images, the Dual Contouring method [22] generates dual meshes from an octree structure. Tetrahedral meshes for complicated domains with topology ambiguity can be generated by splitting the ambiguous leaf cells into tetrahedra and analyzing the edges of these tetrahedra [25]. A parallel Image-to-Mesh conversion algorithm [7] was proposed to generate quality tetrahedral meshes via dynamic point insertions and removals. However, it is still challenging to generate quality finite element meshes directly from raw images bridging image segmentation and mesh generation.

It is also crucial to improve the mesh quality in order to avoid the ill-conditioned linear systems during the finite element analysis. Smoothing methods improve mesh quality by relocating vertices without changing the connectivity [8]. However, traditional smoothing techniques are heuristic and sometimes invert or degrade the local elements. To address this problem, optimization-based smoothing methods are proposed, where each node is relocated at the optimum location based on the local gradient of the surrounding element quality [2]. Methods based on local curvature and volume preserving geometric flows are developed to identify and preserve the main surface features [11, 23]. Topological optimization techniques, such as face swapping and edge removal [10], are utilized to improve the node valence and mesh quality. Although there already exist a variety of mesh denoising methods, research on feature preserving denoising remains active due to its challenging nature.

In this paper, we first extend the HEWCVT [9] from 2D to 3D image segmentation and generate compact and connected segments. Based on the segmented image, the Dual Contouring method [22, 25] is then applied to construct tetrahedral meshes by analyzing both material change edges and interior edges. We also develop an anisotropic Giaquinta-Hildebrandt operator (GHO) diffusion flow for surface smoothing and quality improvement, while optimization based smoothing and topological optimizations are applied together. The key contributions of our proposed algorithms include:

1. The 2D HEWCVT [9] is extended to 3D image segmentation, where 3D spatial information is included in order to eliminate the noise effect. By improving the connectivity of each segment, it generates compact and connected segments without leaving isolated voxels and in keeping the connectivity of the structure; and
2. The anisotropic GHO diffusion flow is developed for surface smoothing which preserves surface features while removing the noise with an anisotropic weighting function. Since GHO is defined based on the second fundamental form of the surface, our proposed algorithm is more sensitive to the curvature-related features.

The remainder of this paper is organized as follows: Sect. 2 describes the HEWCVT-based 3D image segmentation. Section 3 explains tetrahedral mesh generation via Dual Contouring method. Section 4 discusses surface smoothing

via the anisotropic GH0 diffusion flow and explains how to improve the quality of tetrahedral meshes. Section 5 shows some results, and Sect. 6 presents conclusions and future work.

2 CVT-Based 3D Image Segmentation

CVT-based clustering methods [5,6] partition discrete data points into non-overlapping clusters with an initialization of generators. It first constructs Voronoi regions by assigning each point to its nearest generator with certain distance metric. For each Voronoi region, we can iteratively calculate its centroid by minimizing a pre-defined energy function until it coincides with the corresponding generator. Inspired by the HEWCVT method [9] for 2D image segmentation, here we extend it to 3D image segmentation.

The input image I is given in the form of function values, $I = \{I(x, y, z)\}$, where x, y, z are indices of X, Y, Z coordinates. Let the dataset $F = \{f_{P(i)}\}_{i=1}^n$ denote all the intensity values $f_{P(i)}$ of the grayscale image, where n is the total number of voxels and $P(i)$ represents the i^{th} voxel in the physical space. Let $C = \{c_l\}_{l=1}^L$ denote a set of Voronoi generators with intensity values, where L is the number of clusters. The Voronoi regions $V = \{V_l\}_{l=1}^L$ in F corresponding to the generators can be obtained by assigning each voxel to the cluster whose generator is the nearest to it according to the distance metric:

$$V_k = \{f_{P(i)} \in F : \text{dist}(f_{P(i)}, c_k) \leq \text{dist}(f_{P(i)}, c_l), \quad \text{for } l = 1, \dots, L\}, \quad (1)$$

where $\text{dist}(f_{P(i)}, c_k) = \sqrt{|f_{P(i)} - c_k|^2 + 2\lambda \hat{n}_k(P(i))}$ measures the edge-weighted distance between $f_{P(i)}$ and c_k in the grayscale space. The edge-weighted term $\hat{n}_k(P(i))$ represents the number of voxels that do not belong to the k^{th} cluster within ω -ring spherical neighbours of $P(i)$, which includes the local 3D spatial information in the physical space. Here we choose a relatively small value of ω ($\omega = 3$) for all the examples in order to reduce the computational cost. Given any set of generators $C = \{c_l\}_{l=1}^L$ and any partition $U = \{U_l\}_{l=1}^L$ of F , we can define the corresponding HEWCVT energy function of $(C; U)$ as

$$E(C; U) = \sum_{i=1}^n \left(L / \sum_{l=1}^L \text{dist}^{-2}(f_{P(i)}, c_l) \right). \quad (2)$$

Note that the HEWCVT energy function uses the edge-weighted distances to all generators for each voxel. It means that all the generators partially influence the harmonic average for each voxel. By taking into account the physical information and using the harmonic form of energy function, HEWCVT is robust to the initialization and can eliminate the noise in the 3D image during the segmentation. To calculate the updated centroids $\{c_k^*\}_{k=1}^L$, we minimize the HEWCVT energy function with respect to the generators c_k ($k = 1, \dots, L$). If the generators of the Voronoi regions $\{V_l\}_{l=1}^L$ of F equal to their corresponding centroids,

i.e., $c_l = c_l^*$ for $l = 1, \dots, L$, then we call the Voronoi tessellation $\{V_l\}_{l=1}^L$ a centroidal Voronoi tessellation of F . The detailed implementation of HEWCVT-3D is explained as follows:

Algorithm of HEWCVT-3D

Given a 3D image $F = \{f_{P(i)}\}_{i=1}^n$, positive integer L and error tolerance ε ($\varepsilon = 10^{-4}$ in this paper). E_i denotes the HEWCVT energy in the i^{th} iteration. Then perform the following:

1. For each voxel, find its ω -ring neighbouring voxels in advance. Choose L random voxels in the image and take their intensity values as the initialization of the generators $\{c_l\}_{l=1}^L$;
2. Determine the edge-weighted Voronoi clusters $\{V_l\}_{l=1}^L$ of F associated with $\{c_l\}_{l=1}^L$ by (1). For each cluster V_l ($l = 1, \dots, L$), update the cluster centroid c_l^* by minimizing the HEWCVT clustering energy function;
3. If $\frac{E_{i+1} - E_i}{E_i} < \varepsilon$ is reached, return $(\{c_l\}_{l=1}^L; \{V_l\}_{l=1}^L)$; otherwise, set $c_l = c_l^*$ for $l = 1, \dots, L$ and return to Step 2.
4. Merge small isolated segments to its neighbouring cluster with the longest boundary.

We have tested our HEWCVT-based 3D image segmentation algorithm on a 3D MRI Brain-1 image ($181 \times 217 \times 181$) from BrainWeb dataset [4], with 3% noise and 20% intensity non-uniformity (INU), shown in Fig. 1. We segmented the 3D image into four clusters in order to extract the gray matter, white matter, cerebrospinal fluid and background. Figure 1(b) shows the HEWCVT-3D segmentation result after 20 iterations, where neighbouring clusters are rendered with different colors. Figure 1(c) and (d) show the segmented white matter and gray matter, respectively. We also compared our result with EWCVT-3D by extending EWCVT [20] to 3D image domain. From the slice 103 and corresponding segmented images in Fig. 1(e–h), we can observe that HEWCVT-3D yields more accurate results in many regions and both of them can eliminate the noise effect. Figure 1(i) shows the energy convergence curves for both EWCVT-3D and HEWCVT-3D under the same initialization. Compared to EWCVT-3D, the HEWCVT-3D energy converges faster to the minimum. We also segmented the image with 100 different random initializations using both EWCVT-3D and HEWCVT-3D, and the minimized energy outputs are shown in Fig. 1(j). We can observe that HEWCVT-3D is much more stable and less sensitive to initializations than the EWCVT-3D.

Remark 2.1. Compared to the EWCVT-3D, the HEWCVT-3D yields more accurate results by imposing a soft membership function with a harmonic average form of energy function. By taking into account the local 3D spatial information of each voxel, HEWCVT-3D is robust to eliminate the noise effect during the segmentation process. By improving the connectivity of each segment, our HEWCVT-3D can automatically and robustly generate compact segments without leaving isolated voxels. The segmented image can be used to generate tetrahedral meshes directly via the Dual Contouring method [22].

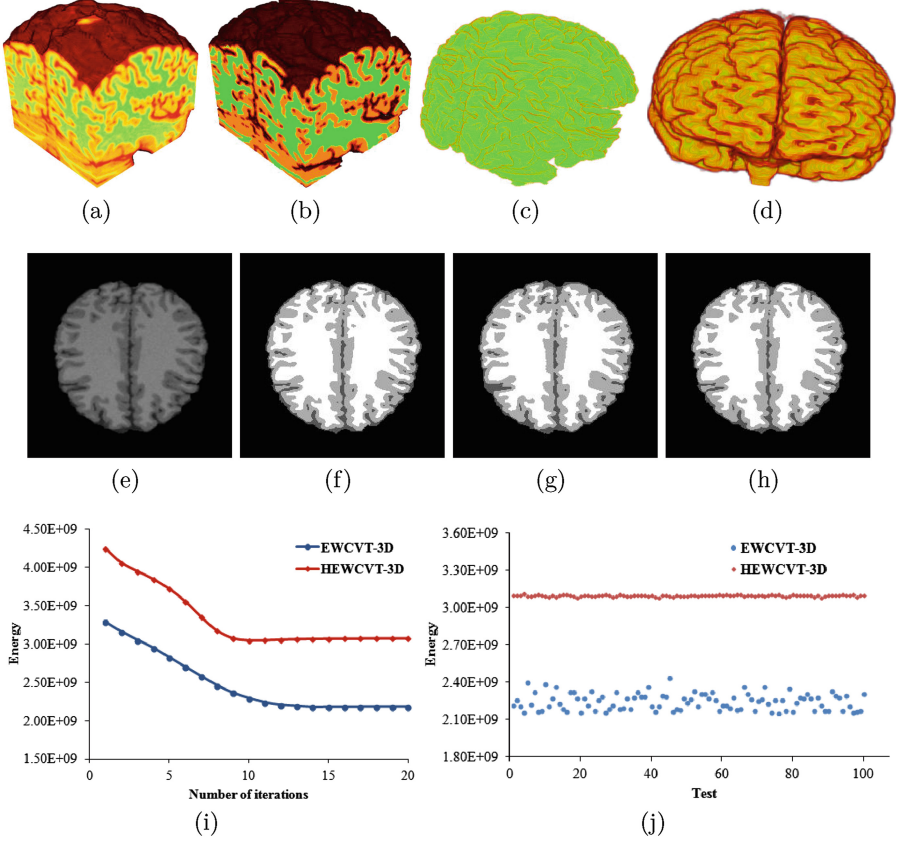


Fig. 1. Segmentation result of the Brain-1 image with 3% noise and 20% INU. (a) Input 3D image; (b) HEWCVT-3D segmentation result; (c) segmented white matter; (d) segmented gray matter; (e-h) the original image, ground truth, EWCVT-3D and HEWCVT-3D results of the slice 103, respectively; (i) energy outputs; and (j) minimized energy outputs of 100 initializations.

3 Tetrahedral Mesh Generation

After the segmentation, we set the image I as a scalar function, $I(x, y, z) \rightarrow J$, where $J = \{0, 1, \dots, L-1\}$ is a set of labels where 0 represents the background and $1, \dots, L-1$ represent the other materials. Based on the labelled image, we analyze both material changes edges and interior edges to generate tetrahedral meshes by using the Dual Contouring method [22, 24, 25]. A *material change edge* is defined as an edge whose two end points have different label indices. An *interior edge* is an edge whose two end points have the same label. Each material change edge belongs to a boundary cell, while interior cells only contain interior edges. For each octree cell, a dual vertex is generated and the tetrahedral mesh is constructed by connecting the dual vertices with octree grids. For each

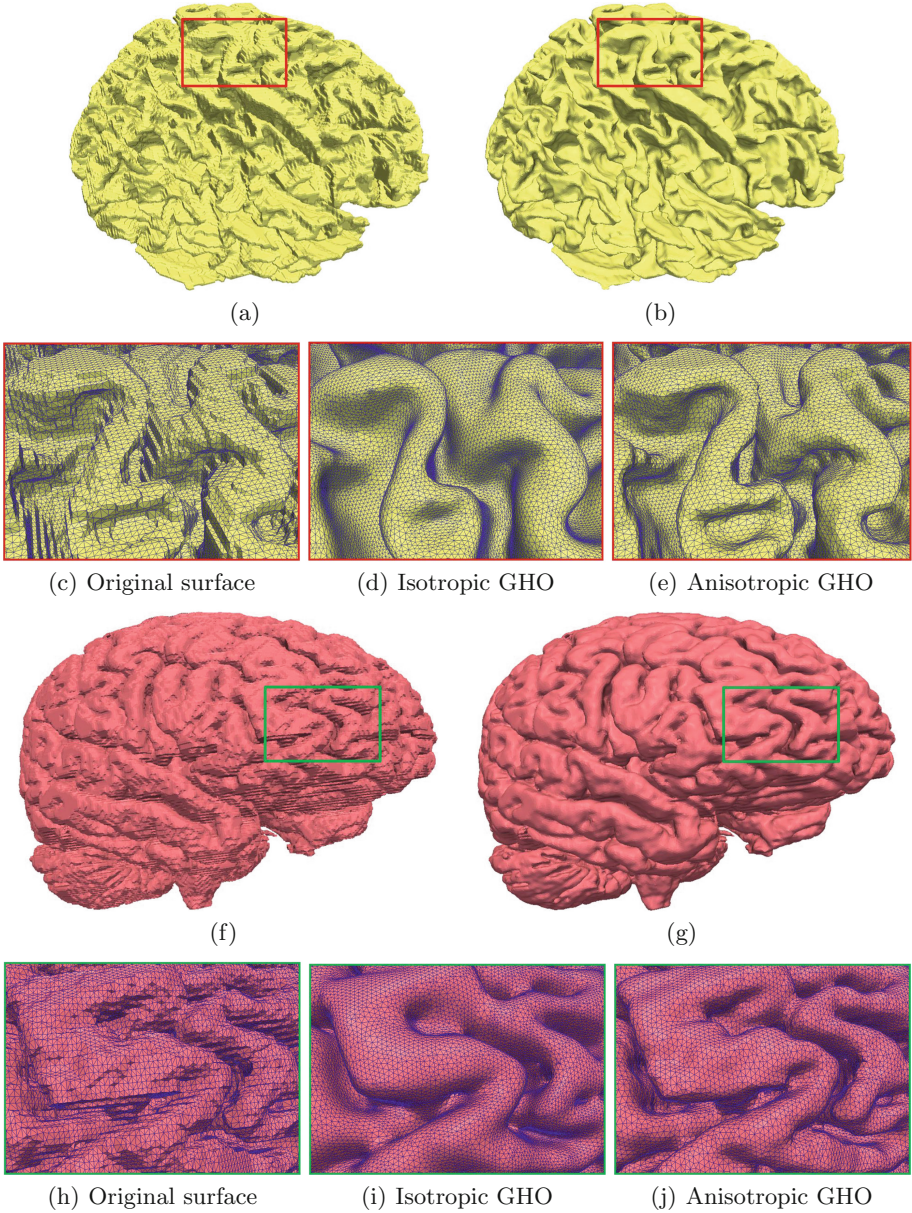


Fig. 2. Tetrahedral meshes. (a, b) The original and smoothed meshes (using anisotropic GHF) of the white matter, respectively; (c) enlargement of the red window in (a); (d, e) zoom-in pictures showing smoothed results of isotropic and anisotropic GHF flow, respectively; (f, g) the original and smoothed meshes (using anisotropic GHF) of the gray matter, respectively; (h) enlargement of the green window in (f); and (i, j) zoom-in pictures showing smoothed results of isotropic and anisotropic GHF flow, respectively. (Color figure online)

boundary cell, we calculate the mass center as the dual vertex. The mass center is defined as the average of all the middle points of the material change edges in the cell. The cell center is simply selected as the dual vertex for each interior cell. For each material change edge, we first find out all its four surrounding leaf cells and corresponding dual vertices. These four dual vertices and the interior grid point of this edge construct a pyramid. For each interior edge, we also obtain four dual vertices. These four dual vertices and two endpoints of this edge form a diamond. Finally, the pyramids and diamonds can be split into four or two tetrahedra. To handle topology ambiguities, a trilinear function can be introduced to detect the ambiguous cells [25]. The ambiguous cells are split into tetrahedra, and tetrahedral meshes are then generated by analyzing the edges of these tetrahedra. Mesh adaptation can be achieved via an adaptive octree data structure [25]. Since the function values $I(x, y, z)$ of the segmented images are discontinuous, the surfaces of the generated tetrahedral meshes are bumpy. Figure 2(a) and (f) show the initial tetrahedral meshes of the white matter and gray matter of the Brain-1, where red/green windows in Fig. 2(c) and (h) highlight the bumpy surfaces. A surface smoothing technique is needed during the following mesh quality improvement.

4 GHO-Based Geometric Flow and Quality Improvement

In the meshes generated from the above algorithm, some elements around the boundaries may have poor aspect ratio, therefore the mesh quality needs to be improved. There are two kinds of vertices in 3D meshes, boundary vertices and interior vertices. For each boundary vertex, we use geometric flow to denoise the surface and improve the quality. The quality of interior tetrahedra is simultaneously improved by using the optimization-based smoothing and topological optimizations.

Laplacian smoothing is the most commonly used mesh smoothing method which iteratively adjusts the vertex to the geometric center of its neighboring vertices. However, it also produces a shrinking effect and an oversmoothing result. Here we develop a new GHO based geometric flow to smooth the surface, which can preserve the concave/convex features and avoid volume shrinkage. Let $S = \{\mathbf{x}(u, v), (u, v) \in \mathbb{R}^2\}$ be a smooth parametric surface in \mathbb{R}^3 . Note that (u, v) can also be written as (u^1, u^2) for convenience. The coefficients of the first fundamental form of S are defined as $g_{\alpha\beta} = \langle \mathbf{x}_{u^\alpha}, \mathbf{x}_{u^\beta} \rangle$ ($\alpha, \beta = 1, 2$), where $\mathbf{x}_{u^\alpha} = \frac{\partial \mathbf{x}}{\partial u^\alpha}$ and $\mathbf{x}_{u^\beta} = \frac{\partial \mathbf{x}}{\partial u^\beta}$. The coefficients of the second fundamental form of S are defined as $b_{\alpha\beta} = \langle \mathbf{n}, \mathbf{x}_{u^\alpha u^\beta} \rangle$, where $\mathbf{x}_{u^\alpha u^\beta} = \frac{\partial^2 \mathbf{x}}{\partial u^\alpha \partial u^\beta}$ and $\mathbf{n} = (\mathbf{x}_u \times \mathbf{x}_v) / \|\mathbf{x}_u \times \mathbf{x}_v\|$. Let $g = \det[g_{\alpha\beta}]$, $[g^{\alpha\beta}] = [g_{\alpha\beta}]^{-1}$, and $[b^{\alpha\beta}] = [b_{\alpha\beta}]^{-1}$. The mean curvature H and Gaussian curvature K can be given by $H = \frac{b_{11}g_{22} - 2b_{12}g_{12} + b_{22}g_{11}}{2g}$ and $K = \frac{b_{11}b_{22} - b_{12}^2}{g}$. Let $f \in C^2(S)$, the Giaquinta-Hildebrandt operator (GHO) acting on $\frac{g}{f}$ is defined as

$$\square f = \operatorname{div}(\diamond f) = \frac{1}{\sqrt{g}} \left[\frac{\partial}{\partial u}, \frac{\partial}{\partial v} \right] \left[\sqrt{g} K [b^{\alpha\beta}] [f_u, f_v]^T \right], \quad (3)$$

where $\text{div}(\mathbf{v})$ is the tangential divergence operator acting on a C^1 smooth vector field \mathbf{v} and \diamond is the second tangential operator (STO) given by

$$\diamond f = [\mathbf{x}_u, \mathbf{x}_v] K [b^{\alpha\beta}] [f_u, f_v]^T. \quad (4)$$

To preserve the volume, we define a surface diffusion flow using the GH0 as

$$\frac{\partial \mathbf{x}}{\partial t} = \text{sign}(K(\mathbf{x})) \square H(\mathbf{x}) \mathbf{n}(\mathbf{x}). \quad (5)$$

Let $S(t)$ be the smoothed surface at $t \geq 0$. Let $A(t)$ denote the area of $S(t)$, $V(t)$ denote the volume of the region enclosed by $S(t)$. Then we have

$$\frac{dA(t)}{dt} = \int_{S(t)} \square H H d\sigma, \quad \frac{dV(t)}{dt} = \int_{S(t)} \square P H d\sigma. \quad (6)$$

Green's Formula [21]: Let $\mathbf{v} = (v_1, v_2, v_3)^T$ be a vector field on S and $f \in C^1(S)$ with compact support. Then

$$\int_S \langle \mathbf{v}, \nabla f \rangle dA = - \int_S f \text{div}(\mathbf{v}) dA, \quad (7)$$

where $\nabla f = [\mathbf{x}_u, \mathbf{x}_v] [g^{\alpha\beta}] [f_u, f_v]^T$ is the tangential gradient operator acting on f . According to the Green's formula, we have

$$\frac{dA(t)}{dt} = \int_{S(t)} \square H H d\sigma = - \int_{S(t)} (\nabla H)^T \diamond H d\sigma, \quad (8)$$

and

$$\frac{dV(t)}{dt} = \int_{S(t)} \square H d\sigma = - \int_{S(t)} (\diamond H)^T \nabla(1) d\sigma = 0. \quad (9)$$

Hence, the proposed geometric flow is volume preserving. Since GH0 is defined based on the second fundamental form of the surface, it is more sensitive to the curvature-related features. From the definition of \diamond and div , we can derive that

$$\square f = g_u^\square f_u + g_v^\square f_v + g_{uu}^\square f_{uu} + g_{uv}^\square f_{uv} + g_v^\square f_v, \quad (10)$$

where

$$\begin{aligned} g_u^\square &= -[b_{11}(g_{22}g_{122} - g_{12}g_{222}) + 2b_{12}(g_{12}g_{212} - g_{22}g_{112}) + b_{22}(g_{22}g_{111} - g_{12}g_{211})] / g^2, \\ g_v^\square &= -[b_{11}(g_{11}g_{222} - g_{12}g_{122}) + 2b_{12}(g_{12}g_{112} - g_{11}g_{212}) + b_{22}(g_{11}g_{211} - g_{12}g_{111})] / g^2, \\ g_{uu}^\square &= b_{22} / g, \quad g_{uv}^\square = -2b_{12} / g, \quad g_{vv}^\square = b_{11} / g, \end{aligned}$$

and $g_{\alpha\beta\gamma} = \langle \mathbf{x}_{u^\alpha}, \mathbf{x}_{u^\beta u^\gamma} \rangle$. Since b_{ij} involves the second order derivatives of the surface, a C^2 -continuous surface representation is required. In this section, the Loop subdivision basis functions are adopted to evolve the surface.

The above geometric flow smooths the surface by moving the vertex along its normal direction. The isotropic smoothing in Eq. (5) can eliminate noise but also smooth out important features. To preserve surface features while removing the noise, we introduce an anisotropic weight $\chi(\mathbf{x})$ for each vertex by using a function of its two principal curvatures, k_1 and k_2 [12]. In order to improve the aspect ratio of the surface mesh, we also add a tangent movement in Eq. (5),

$$\frac{\partial \mathbf{x}}{\partial t} = \chi(\mathbf{x}) \text{sign}(K(\mathbf{x})) \square H(\mathbf{x}) \mathbf{n}(\mathbf{x}) + v(\mathbf{x}) \mathbf{T}(\mathbf{x}), \quad (11)$$

where

$$\chi(\mathbf{x}) = \begin{cases} 1 & \text{if } |k_1| \leq T \text{ and } |k_2| \leq T & \text{Case 1,} \\ 0 & \text{else if } |k_1| > T \text{ and } |k_2| > T \text{ and } K > 0 & \text{Case 2,} \\ k_1 / (H |K|) & \text{else if } |k_1| = \min(|k_1|, |k_2|, |H|) & \text{Case 3,} \\ k_2 / (H |K|) & \text{else if } |k_2| = \min(|k_1|, |k_2|, |H|) & \text{Case 4,} \\ 1 / |K| & \text{else if } |H| = \min(|k_1|, |k_2|, |H|) & \text{Case 5,} \end{cases}$$

and T is a user-defined constant (here we select $T = 0.01$). Case 1 is used to detect uniformly noisy regions, which will be smoothed isotropically. Concave/convex features (case 2) will not be smoothed. We also smooth features detected by cases 3–5 with a speed proportional to the minimum curvature and $|K|$ is used to scale the speed of the movement. $v(\mathbf{x})$ is the velocity in the tangent direction $\mathbf{T}(\mathbf{x})$, which controls the strength of the regularization. We first calculate the mass center $m(\mathbf{x})$ for each vertex on the surface, and then project the vector $m(\mathbf{x}) - \mathbf{x}$ onto the tangent plane to obtain $\mathbf{T}(\mathbf{x})$. If the surface has no noise, we can only apply the tangent movement $v(\mathbf{x})\mathbf{T}(\mathbf{x})$ to improve the aspect ratio of the surface while ignoring the vertex normal movement. Equation (11) is solved over triangular surfaces using Loop subdivision based isogeometric analysis [14].

The surface smoothing via GH0-based geometric flow improves the quality of the surface, but the quality of interior mesh also needs to be improved. To measure tetrahedral mesh quality, we choose three metrics [10]: $Q_1 = \theta_{\min}$, the minimal dihedral angle of each element; $Q_2 = \theta_{\max}$, the maximal dihedral angle of each element; and $Q_3 = 8 \cdot 3^{\frac{5}{2}} V \left(\sum_{j=1}^6 e_j^2 \right)^{-\frac{3}{2}}$, the Joe-Liu parameter, where $\{e_j\}_{j=1}^6$ are six edge lengths, and V is the volume of each tetrahedron. Three techniques are applied to improve the mesh quality: optimization-based mesh smoothing, face swapping and edge removal [10]. The optimization-based

smoothing improves all tetrahedra in the mesh by minimizing the objective function $\epsilon = \sum_{\eta \in \tau} \max(\frac{1}{Q_\eta} - q, 0)^p$, where τ is the set of tetrahedra in the mesh, Q_η represents Joe-Liu value of a tetrahedron $\eta \in \tau$, and q and p are parameters. This approach can improve the overall mesh quality efficiently, but some elements still have poor quality because of the bad valence. Face swapping removes edges with valence 3 or 4 by reconnecting vertices of some elements. Edge removal removes poor quality elements by replacing one ring neighboring tetrahedra of the edge with new tetrahedra with higher quality. Figure 2(b) and (g) show the improved tetrahedral meshes of the white matter and gray matter of the Brain-1 model. Both isotropic and anisotropic GH0 diffusion flow are applied to denoise the bumpy surface with the same temporal step size ($t = 0.02$) and iteration number (100 iterations). As shown in Fig. 2(d) and (i), the isotropic GH0 diffusion flow smooths out the noise but also blurs the surface features. Compared to the isotropic GH0 diffusion flow, it is obvious that our anisotropic GH0 diffusion flow better preserves surface features while removing the noise, see Fig. 2(e, j).

Remark 4.1. Since GH0 is defined based on the second fundamental form of the surface, it is more sensitive to curvature related surface features, such as concave creases and convex ridges. However, isotropic geometric flow smooths out important features while reducing the noise. By introducing an anisotropic weighting function which penalizes surface vertices with a large ratio between their two principal curvatures, the anisotropic GH0 diffusion flow preserves concave and convex features such as brain wrinkles while removing the noise.

5 Results and Discussion

In this section, we apply our presented algorithms to eight 3D medical images that are either noise free or corrupted by different types of noises. All the results were computed on a PC equipped with a 2.93 GHz Intel X3470 CPU and 8 GB of Memory. Statistics of all tested models are given in Table 1. For HEWCVT-3D based image segmentation, we need to define two parameters: L , the number of clusters; and λ , the weighting parameter that balances the clustering energy and the edge-weighted energy.

We tested our HEWCVT-based 3D image segmentation algorithm on eight 3D MRI brain images ($181 \times 217 \times 181$) from BrainWeb [4], with four levels of noise (3%, 5%, 7%, 9%) and two levels of INU (20%, 40%). We segmented each 3D image into four clusters in order to extract the gray matter, white matter, cerebrospinal fluid and background. Figure 3(a) shows the initial Brain-6 3D image with 7% noise and 40% INU, where the slice 106 in both 3D and 2D domains are highlighted in Fig. 3(b). Figure 3(c) shows the HEWCVT-3D based image segmentation, where the green part represent the white matter. We can observe that the noise effect can be well removed during segmentation. We also compared all results with two other methods: k -means [15] and EWCVT-3D [20]; see Fig. 3(d–k). HEWCVT-3D generates better segmentation results without leaving isolated voxels and in keeping the connectivity of the structure,

Table 1. Image segmentation statistics of all tested models.

Image		Brain-1	Brain-2	Brain-3	Brain-4	Brain-5	Brain-6	Brain-7	Brain-8
Noise level		3%	3%	5%	5%	7%	7%	9%	9%
INU level		20%	40%	20%	40%	20%	40%	20%	40%
Number of clusters		4	4	4	4	4	4	4	4
λ		0.05	0.05	0.10	0.10	0.15	0.20	0.30	0.30
Average SA	k -means	74.38%	73.26%	69.78%	69.24%	68.84%	67.97%	67.46%	66.37%
	EWCVT-3D	89.45%	88.68%	84.49%	86.65%	85.13%	83.28%	81.69%	78.43%
	HEWCVT-3D	93.23%	93.12%	92.88%	92.26%	92.24%	91.56%	90.96%	89.26%
Average BR	k -means	79.88%	76.96%	74.18%	73.24%	72.89%	72.47%	71.86%	71.64%
	EWCVT-3D	91.25%	90.98%	89.69%	89.25%	88.62%	86.29%	83.57%	81.45%
	HEWCVT-3D	95.28%	95.11%	94.89%	94.66%	93.84%	92.99%	92.16%	91.83%
SCV	k -means	13.79%	13.94%	14.22%	14.79%	15.03%	15.87%	16.24%	16.63%
	EWCVT-3D	11.96%	12.63%	12.99%	13.78%	13.98%	14.77%	15.21%	15.68%
	HEWCVT-3D	0.78%	0.78%	0.79%	0.82%	0.85%	0.88%	0.90%	0.93%
Average time (seconds)	k -means	35.2	35.4	35.6	34.8	35.2	35.3	34.2	35.4
	EWCVT-3D	45.2	46.4	45.7	44.9	45.6	45.4	44.9	45.5
	HEWCVT-3D	65.8	65.9	66.7	67.8	66.2	68.3	67.9	68.1

while k -means is not robust to handle the noise effect and EWCVT-3D may generate inaccurate results. We first use the segmentation accuracy (SA) [9] to quantitatively evaluate the segmentation results. Given the segmented image B and the ground truth image G obtained from BrainWeb dataset, the SA can be defined as:

$$SA = \frac{N_{Correct}}{N_{Total}} \times 100\%, \quad (12)$$

where $N_{Correct}$ represents the number of correctly classified voxels and N_{Total} is the total number of voxels in the image. In order to evaluate the accuracy of feature preservation, we also use the boundary recall (BR) [16] to measure the portion of boundary voxels in the ground truth that are also identified as boundary by the segmentation being evaluated. The BR can be defined as:

$$BR = \frac{TP}{TP + FN} \times 100\%, \quad (13)$$

where TP is the number of boundary voxels in G with at least one boundary voxel in R in range of two voxels, FN is the number of boundary voxels in G with no boundary voxel in R in range of two voxels. Large SA and BR values are usually considered high accuracy. We also introduce another metric named the segmentation coefficient of variation (SCV) to evaluate the stability of different methods. For each brain image, we test N ($N = 100$ in this paper) random initializations of the generators by using k -means, EWCVT-3D and HEWCVT-3D. We can get one minimized energy value for each test and the SCV can be defined as:

$$SCV = \frac{\sqrt{\frac{1}{N} \sum_{i=1}^N (MinE_i - \overline{MinE})^2}}{\overline{MinE}} \times 100\%, \quad (14)$$

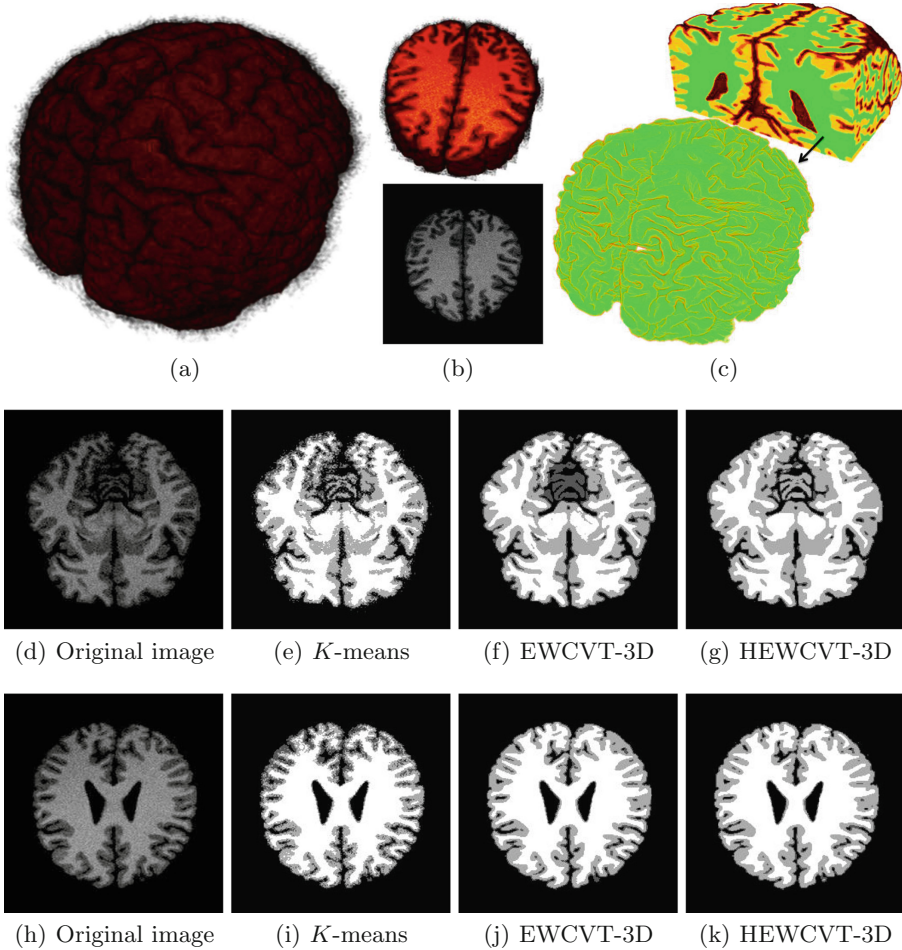


Fig. 3. Brain-6 model. (a) Input image; (b) slice 106; (c) HEWCVT-3D based segmentation; (d–g) and (h–k) from left to right: slices of original data, corresponding slices segmented applying k -means, EWCVT-3D, and HEWCVT-3D.

where $MinE_i$ represents the minimized energy for the i^{th} test, and \overline{MinE} represents the mean of the minimized energy. Large SCV values are usually considered high-variance, otherwise low-variance. The average SA , the average BR and SCV values of the each image with 100 tests are listed in Table 1. We can observe that HEWCVT-3D improves the segmentation accuracy compared to k -means and EWCVT-3D. From the comparison of BR values, it is evident that HEWCVT-3D can also better preserve the connectivity of structure compared to the other two methods. With different initializations, the energy function converges to different values for k -means and EWCVT-3D, while HEWCVT-3D is much more stable and less sensitive to initializations with all $SCVs < 1\%$. In

addition, our HEWCVT-3D method is also robust to noise since the SA , BR and SCV values do not change much for different levels of noise and INU. Since HEWCVT-3D updates cluster centroids by calculating distances to all centroids for each voxel, the computational cost is higher than the other two methods.

Tetrahedral meshes consisting of the white matter, gray matter and cerebrospinal fluid are generated and the mesh quality is improved via geometric flow based smoothing and optimization. Table 2 shows the meshing results for each model. Figure 4(b) shows the improved mesh of Brain-6 with the white matter (yellow), gray matter (red) and cerebrospinal fluid (blue). The improved mesh is in good quality with an dihedral angle range of $(15.11^\circ, 167.17^\circ)$. From the zoom-in pictures we can observe that smoothness and regularity of boundary surfaces between different materials are significantly improved. Figure 4(d, e) and (f, g) show the improved meshes of the white matter and gray matter, respectively, with mesh adaptation highlighted in zoom-in pictures. We can observe that surface features are well preserved during the surface denoising via the anisotropic GH0 diffusion flow.

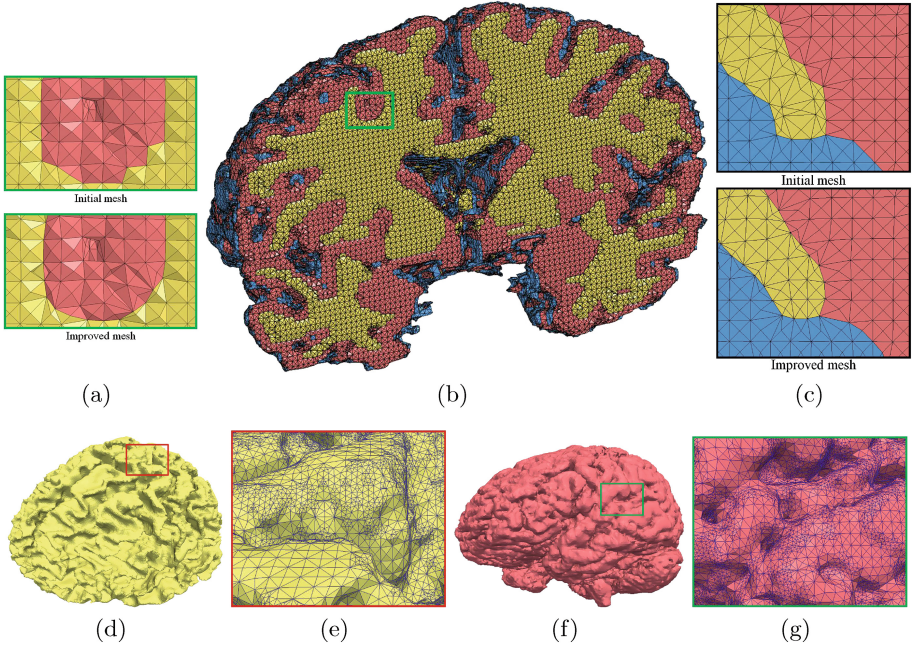


Fig. 4. Tetrahedral mesh of the Brain-6 model. (a, b) Cross section of the final tetrahedral mesh, with zoom-in pictures of the initial and improved meshes of the green box; (c) zoom-in pictures of the initial and improved meshes with three neighboring materials (d) improved tetrahedral mesh of the white matter; (e) enlargement of the red window in (d); (f) improved tetrahedral mesh of the gray matter; and (g) enlargement of the green window in (f). (Color figure online)

Table 2. Mesh statistics of all tested models.

Image	Mesh size (vertices, elements)	Joe-Liu (min, max)	Dihedral angle (min, max)	Time (seconds)
Brain-1	(368,584, 1,796,748)	(0.12, 1.0)	(15.14°, 166.56°)	189.7
Brain-2	(326,576, 1,616,551)	(0.13, 1.0)	(15.10°, 166.94°)	187.8
Brain-3	(332,681, 1,630,137)	(0.12, 1.0)	(15.11°, 167.39°)	184.7
Brain-4	(343,268, 1,682,014)	(0.12, 1.0)	(15.06°, 167.39°)	186.9
Brain-5	(301,298, 1,491,425)	(0.13, 1.0)	(15.08°, 167.76°)	179.9
Brain-6	(282,352, 1,395,796)	(0.11, 1.0)	(15.11°, 167.17°)	179.6
Brain-7	(312,453, 1,534,144)	(0.12, 1.0)	(15.02°, 167.83°)	188.8
Brain-8	(342,683, 1,686,006)	(0.13, 1.0)	(15.01°, 167.89°)	187.7

6 Conclusions and Future Work

In this paper, we have developed an algorithm to segment 3D images and generate tetrahedral meshes with good quality. Given the input 3D image, we first segment the image by using the HEWCVT-3D algorithm. The Dual Contouring method is then used to extract the initial tetrahedral mesh. To smooth out the noise and improve the quality of the tetrahedral mesh, we developed an anisotropic GH0 diffusion flow. The quality of the interior tetrahedron is also improved via optimization techniques. We have successfully tested our method using several volumetric imaging datasets. In the future, we will extend our geometric flow method to quadrilateral meshes and investigate more anisotropic schemes. We will also parallelize our algorithms and apply to more real applications.

Acknowledgment. The authors would like to thank Tao Liao for useful discussions on quality improvement techniques for tetrahedral mesh. The work of K. Hu and Y. Zhang was supported in part by NSF CAREER Award OCI-1149591. G. Xu was supported in part by NSFC Fund for Creative Research Groups of China under the grant 11321061.

References

1. Arifin, A.Z., Asano, A.: Image segmentation by histogram thresholding using hierarchical cluster analysis. *Pattern Recogn. Lett.* **27**(13), 1515–1521 (2006)
2. Canann, S.A., Tristano, J.R., Staten, M.L.: An approach to combined Laplacian and optimization-based smoothing for triangular, quadrilateral, and quadrilateral meshes. In: 7th International Meshing Roundtable, pp. 479–494 (1998)
3. Chan, T.F., Vese, L.A.: Active contour and segmentation models using geometric PDEs for medical imaging. In: Malladi, R. (ed.) *Geometric Methods in Bio-Medical Image Processing*, pp. 63–75. Springer, Heidelberg (2002)
4. Cocosco, C.A., Kollokian, V., Kwan, R.K.S., Pike, G.B., Evans, A.C.: BrainWeb: online interface to a 3D MRI simulated brain database. *NeuroImage* **5**(4), S425 (1997)

5. Du, Q., Faber, V., Gunzburger, M.: Centroidal Voronoi tessellations: applications and algorithms. *SIAM Rev.* **41**(4), 637–676 (1999)
6. Du, Q., Gunzburger, M., Ju, L., Wang, X.: Centroidal Voronoi tessellation algorithms for image compression, segmentation, and multichannel restoration. *J. Math. Imaging Vis.* **24**(2), 177–194 (2006)
7. Foteinos, P.A., Chrisochoides, N.P.: High quality real-time image-to-mesh conversion for finite element simulations. *J. Parallel Distrib. Comput.* **74**(2), 2123–2140 (2014)
8. Freitag, L.A.: On combining Laplacian and optimization-based mesh smoothing techniques. *AMD-Vol. 220 Trends in Unstructured Mesh Generation*, pp. 37–44 (1997)
9. Hu, K., Zhang, Y.: Image segmentation and adaptive superpixel generation based on harmonic edge-weighted centroidal Voronoi tessellation. *Comput. Methods Biomech. Biomed. Eng.: Imaging Vis.* **4**(2), 46–60 (2016). The Special Issue of CompIMAGE'14
10. Leng, J., Zhang, Y., Xu, G.: A novel geometric flow approach for quality improvement of multi-component tetrahedral meshes. *Comput. Aided Des.* **45**(10), 1182–1197 (2013)
11. Liao, T., Li, X., Xu, G., Zhang, Y.: Secondary Laplace operator and generalized Giaquinta-Hildebrandt operator with applications on surface segmentation and smoothing. *Comput. Aided Des.* **70**, 56–66 (2016). A Special Issue of SIAM Conference on Geometric & Physical Modeling 2015
12. Meyer, M., Desbrun, M., Schröder, P., Barr, A.H.: Discrete differential-geometry operators for triangulated 2-manifolds. In: Hege, H.C., Polthier, K. (eds.) *Visualization and Mathematics III*, pp. 35–57. Springer, Heidelberg (2003)
13. Pal, N.R., Pal, S.K.: A review on image segmentation techniques. *Pattern Recogn.* **26**(9), 1277–1294 (1993)
14. Pan, Q., Xu, G., Xu, G., Zhang, Y.: Isogeometric analysis based on extended Loop's subdivision. *J. Comput. Phys.* **299**, 731–746 (2015)
15. Pappas, T.N.: An adaptive clustering algorithm for image segmentation. *IEEE Trans. Sig. Process.* **40**(4), 901–914 (1992)
16. Ren, X., Malik, J.: Learning a classification model for segmentation. In: *Ninth IEEE International Conference on Computer Vision*, pp. 10–17 (2003)
17. Sijbers, J., Scheunders, P., Verhoye, M., der Linden, A.V., Dyck, D.V., Raman, E.: Watershed-based segmentation of 3D MR data for volume quantization. *Magn. Reson. Imaging* **15**(6), 679–688 (1997)
18. Tobias, O.J., Seara, R.: Image segmentation by histogram thresholding using fuzzy sets. *IEEE Trans. Image Process.* **11**(12), 1457–1465 (2002)
19. Tsuda, A., Filipovic, N., Haberthür, D., Dickie, R., Matsui, Y., Stampanoni, M., Schittny, J.C.: Finite element 3D reconstruction of the pulmonary acinus imaged by synchrotron X-ray tomography. *J. Appl. Physiol.* **105**(3), 964–976 (2008)
20. Wang, J., Ju, L., Wang, X.: An edge-weighted centroidal Voronoi tessellation model for image segmentation. *IEEE Trans. Image Process.* **18**(8), 1844–1858 (2009)
21. Xu, G., Zhang, Q.: A general framework for surface modeling using geometric partial differential equations. *Comput. Aided Geom. Des.* **25**(3), 181–202 (2008)
22. Zhang, Y., Bajaj, C., Sohn, B.S.: 3D finite element meshing from imaging data. *Comput. Methods Appl. Mech. Eng.* **194**, 5083–5106 (2005)
23. Zhang, Y., Bajaj, C., Xu, G.: Surface smoothing and quality improvement of quadrilateral/hexahedral meshes with geometric flow. *Commun. Numer. Methods Eng.* **25**(1), 1–18 (2009)

24. Zhang, Y., Hughes, T., Bajaj, C.: An automatic 3D mesh generation method for domains with multiple materials. *Comput. Methods Appl. Mech. Eng.* **199**(5–8), 405–415 (2010)
25. Zhang, Y., Qian, J.: Resolving topology ambiguity for multiple-material domains. *Comput. Methods Appl. Mech. Eng.* **247**, 166–178 (2012)

Computational Modeling of Objects Presented in
Images. Fundamentals, Methods, and Applications
5th International Symposium, CompIMAGE 2016,
Niagara Falls, NY, USA, September 21-23, 2016,
Revised Selected Papers

Barneva, R.P.; Brimkov, V.E.; Tavares, J.M.R.S. (Eds.)

2017, XII, 259 p. 95 illus., Softcover

ISBN: 978-3-319-54608-7